PHYSICAL REVIEW B **112**, L100302 (2025)

Letter

Effects of four-phonon scattering on phonon hydrodynamics in monolayer graphene

Xun Li,[1,*] Zherui Han,[2] Xiulin Ruan,[2] and Li Shi[1,†]

[1]*Walker Department of Mechanical Engineering and Texas Materials Institute, The University of Texas at Austin, Austin, Texas 78712, USA*
[2]*School of Mechanical Engineering and the Birck Nanotechnology Center, Purdue University, West Lafayette, Indiana 47907-2088, USA*

(Received 30 March 2025; revised 11 August 2025; accepted 4 September 2025; published 23 September 2025)

Prior theoretical studies found a large temperature window around 100 K for hydrodynamic phonon transport to occur in monolayer graphene and other layered materials due to dominant momentum-conserving normal scattering processes. However, these studies have yet to account for high-order phonon scattering processes, especially four-phonon scattering that may play an important role and limit the thermal conductivity of graphene at temperatures above 300 K based on some recent predictions. Here, the predicted four-phonon scattering rates are incorporated into a deviational Monte Carlo solution of the Peierls-Boltzmann equation of phonons in monolayer graphene. The results reveal the apparent weakening of hydrodynamic features, including phonon Poiseuille flow and second sound behaviors, even at 100 K temperature. This effect is connected to the predicted increase of momentum-destroying Umklapp scattering in the calculated four-phonon processes. These findings point to the need for further studies of the effects of high-order phonon scattering, including second-order perturbation theory of three-phonon processes, of various materials in non-Fourier lattice thermal transport phenomena.

DOI: 10.1103/pp9w-jyb3

Introduction. One of the major advances in the recent studies of nanoscale thermal transport has been made in theoretical predictions and experimental findings of hydrodynamic phonon transport phenomena at temperatures above the boiling point of liquid nitrogen [1–5]. Hydrodynamic phonon transport occurs when phonons, the energy quanta of lattice vibration and primary heat carriers in nonmetallic solids, exhibit fluid-like collective quasiparticle transport behaviors, which are distinctly different from common heat carrier diffusion behaviors described by Fourier's law, ballistic transport at a low temperature, and rarely observed phase-coherent interference phenomena of thermal phonons. Similar to molecular flows with momentum (q)-conserving intermolecular scattering processes, this transport regime emerges under conditions where phonon-phonon scattering is dominated by momentum-conserving normal (N) processes among small-momentum phonons instead of momentum-destroying Umklapp (U) processes involving large-momentum modes [6]. Peculiar phenomena such as the phonon Poiseuille flow and second sound have now been observed at significantly higher temperatures in various materials including graphite [4,7–9], $\mathrm{SrTiO_3}$ [10], and germanium [11] than previous reports for solid helium [12,13] and sodium fluoride [14–16].

These experimental observations were motivated by earlier theoretical prediction of phonon hydrodynamics in two-dimensional (2D) materials such as graphene [1,2] and its carbon nanotube cousin [17]. These nanostructures provide a relatively simple model systems for the theoretical understanding of non-Fourier transport phenomena, however, the observation of hydrodynamic phonon transport in graphene and nanotubes has remained an experimental challenge due to the difficulty in transport measurements. In addition, these past theoretical computations of hydrodynamic phonon transport were based on first-order perturbation theory of three-phonon (3-ph) scattering [1,2,18–24] and neglected high-order processes, especially four-phonon (4-ph) processes [25,26].

While such 3-ph scattering theory has been considered adequate for explaining phonon transport phenomena below room temperature, recent theoretical and computational studies demonstrated the significant impact of 4-ph scattering on thermal transport in some materials such as boron arsenide (BAs) [26,27]. Meanwhile, recent calculations [28,29] reported that 4-ph processes could play a leading role in monolayer graphene at room temperature and above. Compared to graphite, graphene exhibits unique reflection symmetry that eliminates anharmonic interatomic force constant (IFC) terms with an odd number of out-of-plane displacement components, forbidding the scattering of an odd number of out-of-plane polarized flexural phonons and increasing the calculated thermal conductivity when only 3-ph processes are considered [30]. However, the absence of interlayer interaction in graphene gives rise to a high density of states of low-frequency gapless flexural phonons [31], resulting in high 4-ph scattering rates. Consequently, inclusion of 4-ph processes in first-principles calculation reduces the thermal conductivity of a suspended monolayer graphene at 300 K below the measurement values for graphite [29], opposite to the findings from prior 3-ph calculations [30,32]. Because several studies [33] have recognized the lack of accurate experimental thermal conductivity data of clean suspended

---

[*] Contact author: xunli1992@gmail.com

[†] Contact author: lishi@mail.utexas.edu

2469-9950/2025/112(10)/L100302(7)

graphene due to experimental challenges, it is premature to use existing measurement results to invalidate this predicted thermal conductivity reduction for monolayer graphene compared to graphite.

This surprising prediction is connected to an increased role of U processes in 4-ph scattering, which may produce large-momentum phonons, compared to the 3-ph case around room temperature in graphene. It is unclear, however, whether 4-ph U processes are still important as the temperature decreases toward the liquid nitrogen range, raising an essential question whether or not 4-ph processes calculated by this recent theoretical method may also alter phonon hydrodynamics around 100 K in graphene compared to prior 3-ph predictions.

In this Letter, we report that hydrodynamic features, including both the phonon Poiseuille flow and second sound, are considerably weakened by the inclusion of the predicted 4-ph scattering rates in a deviational Monte Carlo (MC) solution of the Peierls-Boltzmann equation (PBE) of phonon quasiparticles in monolayer graphene. We start with first-principles calculations based on density functional theory using the Vienna *Ab Initio* Simulation Package [34–36] together with a temperature-dependent effective potential (TDEP) method [37] for temperature-dependent interatomic force constants (IFCs). With the computational method and convergence test described in the Supplemental Material [38] (see also Refs. [39–41] therein), the deviational MC method [7,20,24,42,43] is a numerical solution of the PBE with the use of the phonon dispersion and the full scattering matrix that describes the transition rates between any two phonon modes. The full scattering matrix is calculated from first-order perturbation theory with in-house modified ShengBTE [44] and FourPhonon [45] codes. The diagonal components of the matrix are inversely proportional to the single-mode relaxation time (SMRT), while the off-diagonal elements connect the scattering rate of one mode with nonequilibrium distributions of other modes. Neglecting the off-diagonal components is equivalent to the SMRT approximation, which ignores the nonequilibrium distribution of other modes and is inaccurate when dominant N processes produce a nonzero drift velocity for different interacting phonon modes. Without making the SMRT approximation, the MC method uses the obtained nonequilibrium phonon distribution function in real space, reciprocal space, and time domain to calculate temperature and heat flux distributions so as to investigate the size-dependent phonon Poiseuille flow and time-dependent second sound features.

Results and discussion. Figures 1(a) and 1(b) show the calculated 3-ph and 4-ph scattering rates associated with the diagonal elements of the scattering matrix, which are divided into 3-ph and 4-ph processes with N and U characteristics. At both 100 and 300 K, the calculated scattering rate is larger for the 4-ph N processes than for the 4-ph U processes. However, the difference between the two is smaller than the corresponding N-U separation in the 3-ph scattering rates. While the scattering rates of 4-ph N and 3-ph N processes are on the same order of magnitude, the scattering rates are much higher for 4-ph U processes than for the 3-ph U processes for frequencies below about 4 THz. This result is primarily due to the largely increased U scattering rates for low-lying flexural phonon modes that participate in 4-ph processes [29]. Because these flexural modes make an important contribution to the lattice thermal conductivity, inclusion of 4-ph scattering decreases the calculated thermal conductivity compared to the case with only 3-ph scattering, as shown in Figs. 2(a) and 2(b) for 10-μm-wide graphene ribbons, even as the temperature decreases to 70 K. For these thermal conductivity calculations with a finite q mesh size and finite-width graphene, the results become sensitive to the temperature used for renormalizing the IFCs when 4-ph scattering is accounted for, revealing a more significant effect of the renormalization process on the 4-ph scattering rate than on the 3-ph scattering rate, as shown in Fig. S2 [38]. This finding underscores the importance of obtaining accurate IFCs for accurate quantification of the effects of 4-ph processes. It is worth noting that the finite supercell size (10 × 10 × 1) used in TDEP calculation is insufficient to capture the predicted linearization effect of long-wavelength ZA dispersion [46]. While it remains an outstanding question whether this effect could increase the thermal conductivity of infinitely large suspended graphene above those calculated in a recent work [29], the effect is negligible for the current study of graphene with a finite characteristic size that diminishes the contributions from these long-wavelength modes, as shown in the Supplemental Material Sec. VI [38].

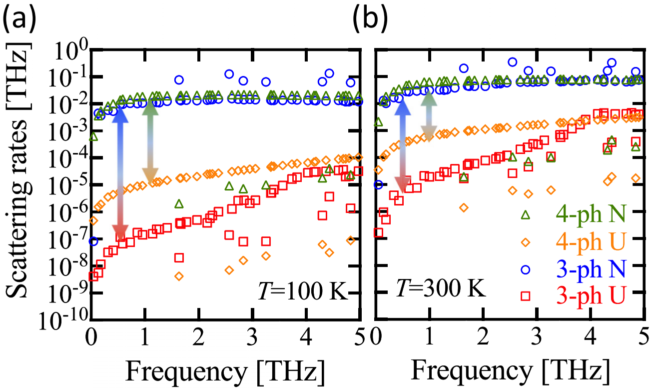

FIG. 1. Calculation results of 3-ph and 4-ph scattering rates at (a) 100 K and (b) 300 K with first-principles IFCs renormalized at the corresponding temperatures. The arrows in (a) and (b) identify the difference between N and U scattering rates for either 3-ph or 4-ph processes. The legend in panel (b) is also applicable to panel (a).

MC simulations of three different configurations are used to investigate the effects of the reduced N-U gap by 4-ph processes on phonon hydrodynamic features, including the phonon Poiseuille flow and second sound. In the first configuration illustrated in Fig. 2(a) for studying a steady-state phonon Poiseuille flow, phonon transport in a graphene ribbon with infinite length and finite width is simulated with a periodic heat flux boundary condition along the length (L) direction and an adiabatic boundary condition in the width (W) direction. The calculated temperature-dependent thermal conductivity for finite-width graphene is shown in Fig. 2(b), where the thermal conductivities peak at a temperature in the range between 80 to 100 K because the finite width limits the phonon mean free paths via diffuse edge scattering. Compared to the calculation that accounts for only 3-ph scattering, both phonon-isotope and 4-ph U scattering decrease the thermal

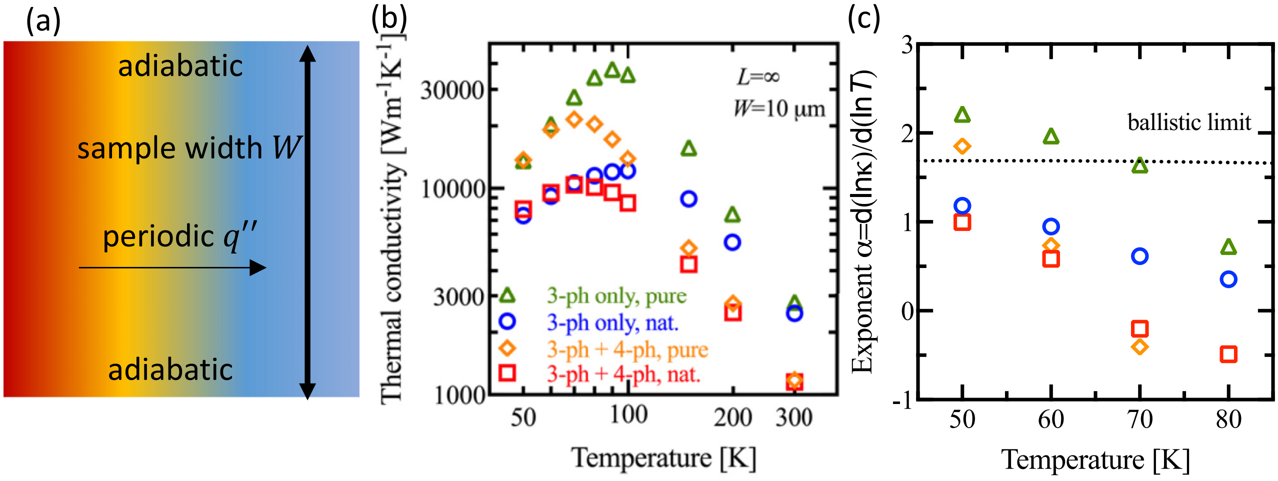

FIG. 2. (a) Schematic illustration of the Monte Carlo simulation domain for investigating phonon transport in a graphene ribbon with adiabatic and diffuse side walls and periodic heat flux (q") condition along the length direction. (b) Calculated temperature-dependent thermal conductivity for graphene ribbons with an infinite length (L), 10-μm width (W), and naturally (nat.) abundance of isotopes or pure ^{13}C isotope. The calculations at 50, 100, 200, and 300 K are performed with first-principles IFCs renormalized at each corresponding temperature. The IFCs at 60 to 90 K and 150 K are obtained by linear interpolation. (c) Extracted temperature (T) dependence of thermal conductivity (κ) defined as $\alpha = \mathrm{d}(\ln\kappa)/\mathrm{d}(\ln T)$. The legends in panel (b) apply to both panels (b) and (c). The error bars in panels (b) and (c) are smaller than the symbol sizes.

conductivity due to their momentum-destroying nature. However, the relevant temperature ranges of the two scattering processes are different. Phonon-isotope scattering is effective at low to intermediate temperatures where overall phonon-phonon scattering is weak. In comparison, 4-ph U processes are usually important at sufficiently high temperatures where optical phonons and large-momentum acoustic modes are thermally populated to participate in such processes and help satisfy the energy and momentum selection rules. However, the effect of 4-ph scattering in the calculated thermal conductivity of graphene is observable even at temperatures as low as 80 K due to the large density of states of low-lying flexural phonons.

To characterize the phonon Poiseuille flow, the exponent of temperature (T) dependence of the thermal conductivity (κ), defined as $\alpha = \mathrm{d}(\ln\kappa)/\mathrm{d}(\ln T)$, is calculated and shown in Fig. 2(c). In isotopically pure samples with only 3-ph scattering accounted for, the calculated thermal conductivity increases faster than the ballistic limit below 70 K. This peculiar characteristic has been explained from a random-walk picture [21] or by the concept of phonon viscous damping [20] of a phonon Poiseuille flow, where momentum-conserving N processes may increase the effective phonon-boundary scattering mean-free path (MFP) when the sample width is larger than the average MFP of N processes and smaller than the mean free paths of U processes [47]. As a result, the heat flux exhibits a parabolic profile across the width as shown in Fig. S4 [38]. For natural samples with 0.1% of ^{13}C, the temperature exponent drops below the ballistic limit due to the momentum-destroying phonon-isotope scattering. When 4-ph scattering is included, the temperature exponent also decreases and drops close to or below the ballistic limit, and the heat flux profile becomes relatively flat in Fig. S4 [38]. This result suggests that the decreased N-U gap by the 4-ph processes diminishes the phonon Poiseuille flow behavior despite the still larger scattering rate for the 4-ph N processes than for the 4-ph U processes.

To guide the other two MC simulations, we calculate the second sound dispersion and attenuation by solving the PBE with the Callaway scattering model that makes the SMRT approximation to evaluate normal and Umklapp scattering rates separately (see details in the Supplemental Material Sec. VIII [38]). Here, the SMRT results obtained from the first-principles calculation in Fig. 1 are used in the Callaway model. For the 3-ph only case, the optimal pulse width for second sound to be observed is determined as 2 ns at 100 K and about 100 ps at 300 K as shown in Fig. S5 [38]. The inclusion of 4-ph scattering makes the conditions more stringent for second sound to occur than the case with only 3-ph scattering.

In the second configuration shown in Fig. 3(a), MC simulations are performed to reveal the transient temperature responses of a ring-shaped pump heating experiment for investigating second sound. Taking advantage of the circular symmetry, only a quarter of the ring-shaped pump setup is simulated with specular conditions at two inner boundaries besides two isothermal outer boundaries that are assumed to be thermally anchored to a heat sink. Changing the outer boundaries to be adiabatic only leads to a small effect on the simulation results, as shown in the Supplemental Material Sec. IX [38]. The actual boundary condition in a possible experimental configuration is expected to fall between the isothermal and adiabatic boundary conditions. For this and the following simulation, Gaussian profiles are used for simulating laser irradiation with parameters adopted from a recent experiment [7]. Figure 3(b) shows the temporal temperature profile at different positions at an ambient temperature of 100 K with a heating pulse duration (τ) of 2 ns, which is

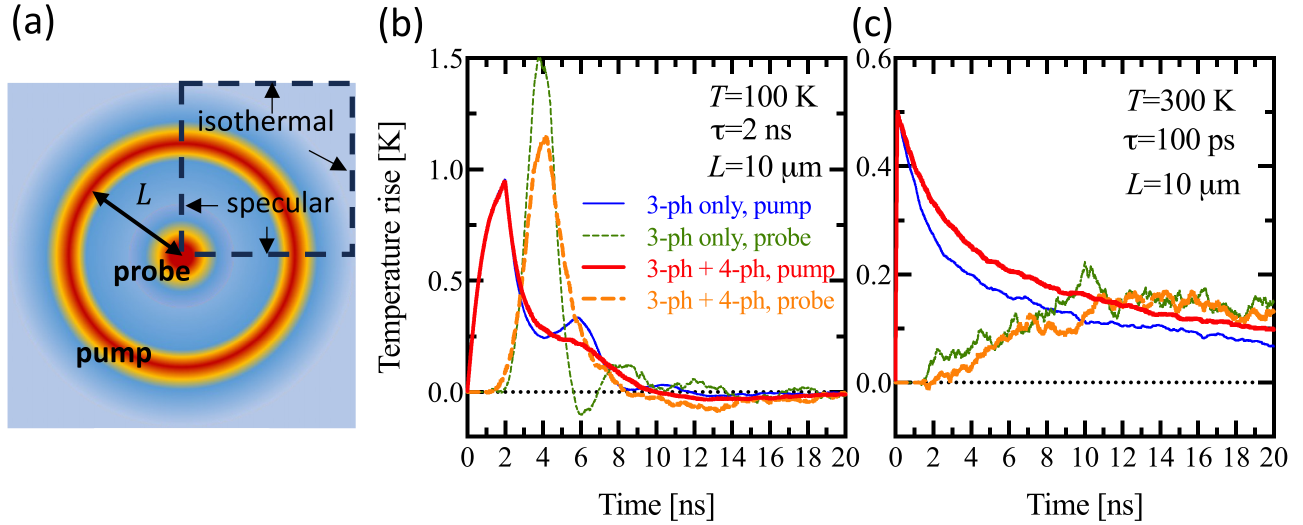

FIG. 3. (a) Schematic illustration of a pump-probe thermal reflectance measurement with a 10-μm radius ring-shaped pump and center probe focused on the natural graphene sample. The simulated box dimension is 15 μm by 15 μm. (b), (c) Calculated transient temperature responses along the ring-shaped region and at the center of the graphene sample as a function of delay time after the pump pulse excitation with a duration (τ) of 2 ns at an ambient temperature of (b) 100 K and (c) 100 ps at 300 K. The legends in panel (b) apply to both panels (b) and (c).

chosen as the inverse of the optimum second sound frequency. When only 3-ph scattering is included in the simulation, the calculated temperature at the center of the probe beam starts to increase and peaks at a delay time near 4 ns. Subsequently, the thermal pulse is reflected back at the center due to an equivalent adiabatic boundary so that the temperature starts to decrease. Interestingly, the temperature drops below the ambient temperature and reaches a local minimum, suggesting a lattice cooling effect, before it oscillates and decays to the ambient temperature. Such lattice cooling effect upon laser irradiation is due to the wave nature of heat propagation that causes oscillation in the calculated phonon temperature below and above the ambient temperature, similar to the appearance of positive and negative pressure in a conventional sound wave in air. Such an effect would only occur in the hydrodynamic phonon transport regime but not in the diffusive or ballistic regime. With only 3-ph scattering accounted for, the calculated lattice cooling and temperature oscillation in graphene are similar to those predicted and observed in a recent pump-probe measurement of graphite with such a ring-shaped pump setup [7]. When 4-ph scattering is accounted for in the Monte Carlo simulation, however, the cooling effect is much reduced and delayed, showing a slower and more diffusion-like response than the 3-ph only case. At 300 K with or without 4-ph scattering, the calculated temperature at the center probe increases with the delay time initially, before it decreases back to the ambient temperature according to the heat diffusion theory after a relatively long delay time compared to the 100 K case.

The temporal temperature profiles along the ring-shaped pump beam are also shown in Figs. 3(b) and 3(c). Upon laser irradiation, the temperature at the location of the pump beam initially increases. When only 3-ph scattering is included at 100 K, the temperature at the pump decreases and oscillates at the end of the 2-ns pump pulse, leaving a local minimum at around 4 ns as shown in Fig. 3(b). The local minimum position is the same as the peak position of the temperature at the center probe location, showing that a heat wave is formed across the 10 μm length. When 4-ph scattering is included in the simulation, in comparison, the temperature reaches the peak and gradually decreases with only small oscillations without exhibiting clear local minima. Such a thermal response is similar to a diffusive thermal decay, which is very clearly shown in Fig. 3(c) at 300 K due to increased U scattering rates.

Monte Carlo simulation is also carried out for the third configuration shown in Fig. 4(a), which represents a transient thermal grating (TTG) measurement of graphene. Figures 4(b) and 4(c) show the calculated temperature responses of the grating pump as a function of delay time upon the pump excitation. When only 3-ph scattering is considered in the simulation at 100 K, the calculated temperature responses at both the peak and valley pump intensity locations exhibit significant oscillating behavior of a heat wave, as shown in Fig. 4(b). The oscillations at the peak and valley intensity locations are out of phase in Fig. 4(b). When the temperature at the peak location reaches a local maximum, the temperature at the valley location shows the local minimum and vice versa. This observed oscillation implies a shift of the peak and valley positions of a standing thermal wave, which can be observed in experiments from the flip of the TTG signal [4,8]. The oscillation is clearly different from a typical monotonic temperature decay at the peak position and increase at the valley location in the diffusive phonon transport regime, which are shown in the calculation results of Fig. 4(c) for 300-K ambient temperature. When 4-ph scattering is accounted for in the simulation, the oscillation amplitude in the calculated temperature responses at 100 K are reduced appreciably and decay to a constant value relatively fast. Just like the simulation results for the ring-shaped pump measurement, this latter result again reveals that the reduced N-U gap by 4-ph scattering considerably suppress the second sound feature in

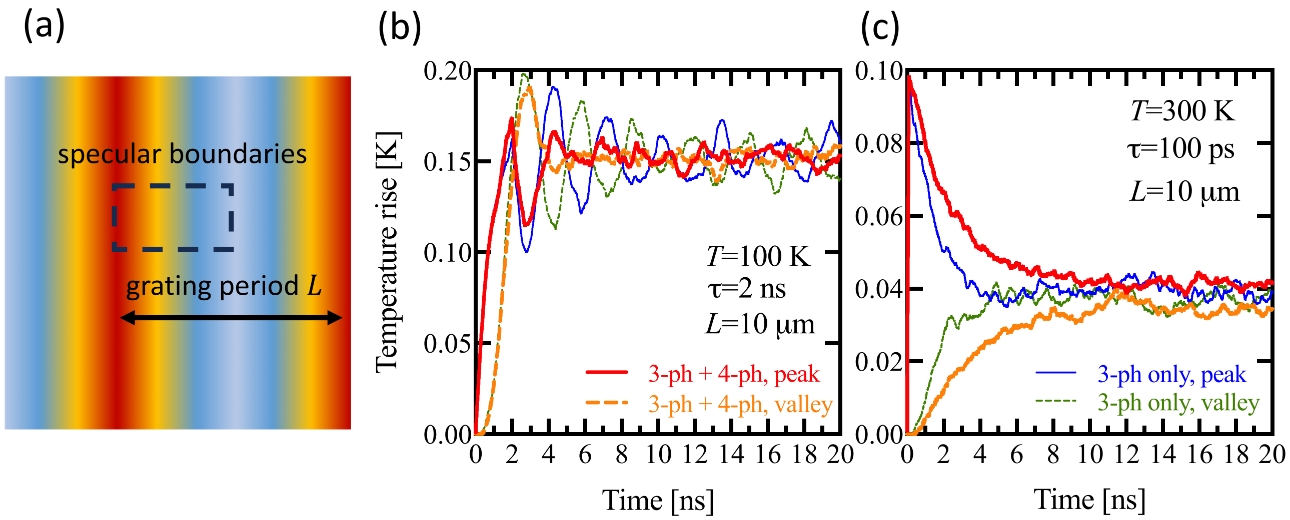

FIG. 4. (a) Schematic illustration of the Monte Carlo simulation domain for a transient thermal grating measurement of graphene. The simulated box dimension is 5 μm by 10 nm. (b), (c) Calculated transient temperature responses of natural graphene at the peak and valley excitation intensity locations of the grating as a function of the delay time from the pulse excitation with a duration (τ) of 2 ns at a temperature of (b) 100 K and (c) 100 ps at 300 K. The legends in panels (b) and (c) apply to both panels (b) and (c).

graphene. These MC results at 100 K agree with analytical solutions of the TTG amplitude [48], which we calculated with our *ab initio* inputs for 3-ph and 4-ph scattering (see details in the Supplemental Material Sec. X [38]). The specular reflection boundaries are used in the TTG simulations due to the one-dimensional periodic heating condition. Thus, there is not a heat sink to absorb the energy from irradiation and the temperature rise in the system would approach a nonzero value as shown in Figs. 4(b) and 4(c).

Conclusion. The Monte Carlo simulation results for these three different configurations consistently show that inclusion of the recently predicted 4-ph scattering rates weakens phonon hydrodynamic features in graphene. Because of the large density of states of flexural phonons, the calculated 4-ph scattering rate is still important in graphene even at temperature as low as 50 K, increasing the Umklapp scattering rate toward the normal scattering rate. Such an increase not only reduces the calculated thermal conductivity below the measured value of graphite, but also weakens the temperature dependence compared to the ballistic limit and the 3-ph case at temperatures near 50 K. Moreover, inclusion of the predicted 4-ph scattering rates considerably reduces lattice cooling and suppress the thermal wave oscillation at 100 K in two second sound measurement configurations, suggesting an important role of 4-ph scattering on examining the possibility of observing phonon hydrodynamics in graphene.

These findings call for further theoretical calculations and experiments to investigate the effects of high-order phonon scattering processes on hydrodynamic phonon transport in graphene and other systems. First-order perturbation theory has been used in this and related works [29] to treat both 3-ph and 4-ph processes. Further studies in second-order perturbation theoretical computation of 3-ph processes are needed to quantify whether this additional second order effect is negligible or not compared to the calculated 4-ph scattering rate [31,49–51], which is also a second-order effect. Further advances are required to overcome the challenges in theoretical computations to account for these and other high-order effects on phonon transport calculations of not only monolayer graphene but also multilayer graphene and graphite, for which experimental data are more available and accepted than for suspended monolayer graphene. Ultimately, the effects of four-phonon scattering and other high-order processes on the thermal transport properties of graphene and related materials will remain an open problem until innovations are made to obtain accurate thermal transport measurement data of this intriguing class of materials.

Acknowledgments. The authors acknowledge two collaborative grants (Grants No. 2321301 and No. 2321302) of the Thermal Transport Processes Program of National Science Foundation and the Texas Advanced Computing Center (TACC) at The University of Texas at Austin for providing computational resources that have contributed to the research results reported within this paper.

Data availability. The data that support the findings of this article are not publicly available upon publication because it is not technically feasible and/or the cost of preparing, depositing, and hosting the data would be prohibitive within the terms of this research project. The data are available from the authors upon reasonable request.

---

[1] S. Lee, D. Broido, K. Esfarjani, and G. Chen, Hydrodynamic phonon transport in suspended graphene, Nat. Commun. **6**, 6290 (2015).

[2] A. Cepellotti, G. Fugallo, L. Paulatto, M. Lazzeri, F. Mauri, and N. Marzari, Phonon hydrodynamics in two-dimensional materials, Nat. Commun. **6**, 6400 (2015).

[3] Y. Guo and M. Wang, Phonon hydrodynamics and its applications in nanoscale heat transport, Phys. Rep. **595**, 1 (2015).

[4] S. Huberman, R. A. Duncan, K. Chen, B. Song, V. Chiloyan, Z. Ding, A. A. Maznev, G. Chen, and K. A. Nelson, Observation of second sound in graphite at temperatures above 100 K, Science **364**, 375 (2019).

[5] S. Lee and X. Li, Hydrodynamic phonon transport: Past, present and prospects, in *Nanoscale Energy Transport*, edited by B. Liao (IOP Publishing, Bristol, 2020), pp. 1–26.

[6] G. Chen, *Nanoscale Energy Transport and Conversion: A Parallel Treatment of Electrons, Molecules, Phonons, and Photons* (Oxford University Press, New York, 2005).

[7] J. Jeong, X. Li, S. Lee, L. Shi, and Y. Wang, Transient hydrodynamic lattice cooling by picosecond laser irradiation of graphite, Phys. Rev. Lett. **127**, 085901 (2021).

[8] Z. Ding, K. Chen, B. Song, J. Shin, A. A. Maznev, K. A. Nelson, and G. Chen, Observation of second sound in graphite over 200 K, Nat. Commun. **13**, 285 (2022).

[9] X. Huang, Y. Guo, Y. Wu, S. Masubuchi, K. Watanabe, T. Taniguchi, Z. Zhang, S. Volz, T. Machida, and M. Nomura, Observation of phonon Poiseuille flow in isotopically purified graphite ribbons, Nat. Commun. **14**, 2044 (2023).

[10] V. Martelli, J. L. Jiménez, M. Continentino, E. Baggio-Saitovitch, and K. Behnia, Thermal transport and phonon hydrodynamics in strontium titanate, Phys. Rev. Lett. **120**, 125901 (2018).

[11] A. Beardo *et al.*, Observation of second sound in a rapidly varying temperature field in Ge, Sci. Adv. **7**, eabg4677 (2021).

[12] L. P. Mezhov-Deglin, Measurement of the thermal conductivity of crystalline He^4, Zh. Eksp. Teor. Fiz. **49**, 66 (1965).

[13] C. C. Ackerman, and W. C. Overton, Second sound in solid helium-3, Phys. Rev. Lett. **22**, 764 (1969).

[14] H. E. Jackson, C. T. Walker, and T. F. McNelly, Second sound in NaF, Phys. Rev. Lett. **25**, 26 (1970).

[15] T. F. McNelly, S. J. Rogers, D. J. Channin, R. J. Rollefson, W. M. Goubau, G. E. Schmidt, J. A. Krumhansl, and R. O. Pohl, Heat Pulses in NaF: Onset of second sound, Phys. Rev. Lett. **24**, 100 (1970).

[16] H. E. Jackson and C. T. Walker, Thermal conductivity, second sound, and phonon-phonon interactions in NaF, Phys. Rev. B **3**, 1428 (1971).

[17] S. Lee and L. Lindsay, Hydrodynamic phonon drift and second sound in a (20,20) single-wall carbon nanotube, Phys. Rev. B **95**, 184304 (2017).

[18] Y. Guo and M. Wang, Phonon hydrodynamics for nanoscale heat transport at ordinary temperatures, Phys. Rev. B **97**, 035421 (2018).

[19] X.-P. Luo, Y.-Y. Guo, M.-R. Wang, and H.-L. Yi, Direct simulation of second sound in graphene by solving the phonon Boltzmann equation via a multiscale scheme, Phys. Rev. B **100**, 155401 (2019).

[20] X. Li and S. Lee, Role of hydrodynamic viscosity on phonon transport in suspended graphene, Phys. Rev. B **97**, 094309 (2018).

[21] Z. Ding, J. Zhou, B. Song, V. Chiloyan, M. Li, T.-H. Liu, and G. Chen, Phonon hydrodynamic heat conduction and Knudsen minimum in graphite, Nano Lett. **18**, 638 (2018).

[22] X. Li and S. Lee, Crossover of ballistic, hydrodynamic, and diffusive phonon transport in suspended graphene, Phys. Rev. B **99**, 085202 (2019).

[23] Y. Guo, Z. Zhang, M. Bescond, S. Xiong, M. Wang, M. Nomura, and S. Volz, Size effect on phonon hydrodynamics in graphite microstructures and nanostructures, Phys. Rev. B **104**, 075450 (2021).

[24] X. Li, H. Lee, E. Ou, S. Lee, and L. Shi, Reexamination of hydrodynamic phonon transport in thin graphite, J. Appl. Phys. **131**, 075104 (2022).

[25] T. Feng and X. Ruan, Quantum mechanical prediction of four-phonon scattering rates and reduced thermal conductivity of solids, Phys. Rev. B **93**, 045202 (2016).

[26] T. Feng, L. Lindsay, and X. Ruan, Four-phonon scattering significantly reduces intrinsic thermal conductivity of solids, Phys. Rev. B **96**, 161201(R) (2017).

[27] F. Tian, B. Song, X. Chen, N. K. Ravichandran, Y. Lv, K. Chen, S. Sullivan, J. Kim, Y. Zhou, and T.-H. Liu, Unusual high thermal conductivity in boron arsenide bulk crystals, Science **361**, 582 (2018).

[28] T. Feng and X. Ruan, Four-phonon scattering reduces intrinsic thermal conductivity of graphene and the contributions from flexural phonons, Phys. Rev. B **97**, 045202 (2018).

[29] Z. Han and X. Ruan, Thermal conductivity of monolayer graphene: Convergent and lower than diamond, Phys. Rev. B **108**, L121412 (2023).

[30] L. Lindsay, D. A. Broido, and N. Mingo, Flexural phonons and thermal transport in graphene, Phys. Rev. B **82**, 115427 (2010).

[31] X. Li and L. Shi, Open problems in transport physics of ultrahigh-thermal conductivity materials, J. Mater. Res. **39**, 2757 (2024).

[32] L. Lindsay, D. A. Broido, and N. Mingo, Flexural phonons and thermal transport in multilayer graphene and graphite, Phys. Rev. B **83**, 235428 (2011).

[33] M. M. Sadeghi, M. T. Pettes, and L. Shi, Thermal transport in graphene, Solid State Commun. **152**, 1321 (2012).

[34] G. Kresse and J. Furthmüller, Efficient iterative schemes for *ab initio* total-energy calculations using a plane-wave basis set, Phys. Rev. B **54**, 11169 (1996).

[35] G. Kresse and J. Furthmüller, Efficiency of ab-initio total energy calculations for metals and semiconductors using a plane-wave basis set, Comput. Mater. Sci. **6**, 15 (1996).

[36] G. Kresse and D. Joubert, From ultrasoft pseudopotentials to the projector augmented-wave method, Phys. Rev. B **59**, 1758 (1999).

[37] O. Hellman, P. Steneteg, I. A. Abrikosov, and S. I. Simak, Temperature dependent effective potential method for accurate free energy calculations of solids, Phys. Rev. B **87**, 104111 (2013).

[38] See Supplemental Material at http://link.aps.org/supplemental/10.1103/pp9w-jyb3 for the computational methods and supplementary figures for thermal conductivity calculations in finite-width samples with interatomic force constants calculated at different temperatures.

[39] C. D. Landon, *A Deviational Monte Carlo Formulation of Ab Initio Phonon Transport and its Application to the Study of Kinetic Effects in Graphene Ribbons*, (Massachusetts Institute of Technology Press, Cambridge, MA, 2014).

[40] J. P. Perdew, K. Burke, and M. Ernzerhof, Generalized gradient approximation made simple, Phys. Rev. Lett. **77**, 3865 (1996).

[41] N. Benshalom, G. Reuveni, R. Korobko, O. Yaffe, and O. Hellman, Dielectric response of rock-salt crystals at finite temperatures from first principles, Phys. Rev. Mater. **6**, 033607 (2022).

[42] J.-P. M. Péraud and N. G. Hadjiconstantinou, Efficient simulation of multidimensional phonon transport using energy-based variance-reduced Monte Carlo formulations, Phys. Rev. B **84**, 205331 (2011).

[43] C. D. Landon and N. G. Hadjiconstantinou, Deviational simulation of phonon transport in graphene ribbons with *ab initio* scattering, J. Appl. Phys. **116**, 163502 (2014).

[44] W. Li, J. Carrete, N. A. Katcho, and N. Mingo, ShengBTE: A solver of the Boltzmann transport equation for phonons, Comput. Phys. Commun. **185**, 1747 (2014).

[45] Z. Han, X. Yang, W. Li, T. Feng, and X. Ruan, Four-Phonon: An extension module to ShengBTE for computing four-phonon scattering rates and thermal conductivity, Comput. Phys. Commun. **270**, 108179 (2022).

[46] E. Mariani and F. Von Oppen, Flexural phonons in free-standing graphene, Phys. Rev. Lett. **100**, 076801 (2008).

[47] D. G. Cahill and R. O. Pohl, Lattice vibrations and heat transport in crystals and glasses, Annu. Rev. Phys. Chem. **39**, 93 (1988).

[48] V. Chiloyan, S. Huberman, Z. Ding, J. Mendoza, A. A. Maznev, K. A. Nelson, and G. Chen, Green's functions of the Boltzmann transport equation with the full scattering matrix for phonon nanoscale transport beyond the relaxation-time approximation, Phys. Rev. B **104**, 245424 (2021).

[49] H. J. Maris, 6 - Interaction of sound waves with thermal phonons in dielectric crystals, in *Physical Acoustics*, edited by W. P. Mason and R. N. Thurston (Academic, New York, 1971), Vol. 8, pp. 279–345.

[50] N. Mingo and D. A. Broido, Length dependence of carbon nanotube thermal conductivity and the "problem of long waves", Nano Lett. **5**, 1221 (2005).

[51] P. Carruthers, Resonance in phonon-phonon scattering, Phys. Rev. **125**, 123 (1962).

Supplemental Material

Effects of four-phonon scattering on phonon hydrodynamics in monolayer graphene

Xun Li,[1,*] Zherui Han,[2] Xiulin Ruan,[2] and Li Shi[1,†]

[1]Walker Department of Mechanical Engineering and Texas Materials Institute, The University of Texas at Austin, Austin, TX 78712, USA

[2]School of Mechanical Engineering and the Birck Nanotechnology Center, Purdue University, West Lafayette, Indiana 47907-2088, USA

[*]corresponding email: xunli1992@gmail.com

[†]corresponding email: lishi@mail.utexas.edu

I. Details of the Monte Carlo simulation

Phonon transport in graphene can be simulated by solving the Peierls-Boltzmann equation (PBE) with a full scattering matrix,

$$\frac{\partial f_i(\mathbf{r},t)}{\partial t} + \mathbf{v}_i \cdot \nabla_{\mathbf{r}} f_i(\mathbf{r},t) = \sum_j C_{ij} f_j(\mathbf{r},t) \tag{S1}$$

where i indicates a phonon state, f is the phonon distribution function, $\mathbf{v}$ is the phonon group velocity, $\mathbf{r}$ is the position vector in the two-dimensional real space, t is time, and C_{ij} is the element of scattering matrix $\mathbf{C}$. The PBE is solved by a deviational Monte Carlo method with inputs of phonon dispersion and scattering matrix from first-principles calculations, which has been used to study steady-state thermal transport in two-dimensional graphene ribbons [1–3] and three-dimensional graphite [4], and transient simulation of second sound in three-dimensional graphite [5]. The details of the algorithm can be found in these prior reports.

The first Brillouin zone of the reciprocal space is discretized with a 40×40×1 grid for all calculations. For the steady-state calculation of thermal conductivity of finite-size ribbon, the real space is discretized into 1×10 control volumes. The time space is discretized with a time interval ranging from 8 ps at 50 K to 1 ps at 300 K. For the second sound simulations, the samples are two-dimensional graphene ribbons with boundary conditions shown in Fig. 4(a) for the pump-probe simulation and Fig. 5(a) for the transient thermal grating simulation. The real space is discretized into 15×15 control volumes for the pump-probe simulation and 10×1 control volumes for the transient thermal grating simulation. The time space is discretized with a time interval of 5 and 1 ps at 100 and 300 K, respectively,

The heating by the pump laser is simulated by applying a heat source to the control volumes for a certain time duration. The intensity of the heat source follows the Gaussian distribution with a full width at half maximum value of 6 μm along the radial direction for the pump-probe simulation and the x direction for the transient thermal grating simulation. In the process of heating, phonons are generated following the equilibrium Bose-Einstein distribution at the local temperature. The time- and space-dependent phonon distribution function is calculated to sample the local temperature.

II. Construction of the full scattering matrix

The three-phonon scattering rates $\Gamma_{ijk}^{\pm}$ and four-phonon scattering rates $\Gamma_{ijkl}^{\pm\pm}$ are calculated as in the ShengBTE [6] and FourPhonon [7] packages with changes in evaluating the delta function in the adaptive Gaussian broadening scheme. The delta function is approximated as in Eqs. (16-18) of the ShengBTE [6] package, except that the summation over reciprocal vector components is carried out only for the in-plane directions in Eq. (18) due to the two-dimensional nature of graphene.

The matrix elements are calculated as [8]

$$C_{ij}^{\mathrm{3ph}} = \sum_{k}\left\{\left[-\Gamma_{ijk}^{+} - \Gamma_{ijk}^{+}\frac{f_i^{\mathrm{eq}}(f_i^{\mathrm{eq}}+1)}{f_j^{\mathrm{eq}}(f_j^{\mathrm{eq}}+1)} + \Gamma_{ijk}^{+}\frac{f_i^{\mathrm{eq}}(f_i^{\mathrm{eq}}+1)}{f_k^{\mathrm{eq}}(f_k^{\mathrm{eq}}+1)}\right] + \frac{1}{2}\left[\Gamma_{ijk}^{-} + \Gamma_{ijk}^{-}\frac{f_i^{\mathrm{eq}}(f_i^{\mathrm{eq}}+1)}{f_j^{\mathrm{eq}}(f_j^{\mathrm{eq}}+1)} + \Gamma_{ijk}^{-}\frac{f_i^{\mathrm{eq}}(f_i^{\mathrm{eq}}+1)}{f_k^{\mathrm{eq}}(f_k^{\mathrm{eq}}+1)}\right]\right\}. \tag{S2}$$

for three-phonon scattering, and

$$C_{ij}^{\mathrm{4ph}} = \sum_{kl}\left\{\frac{1}{2}\left[-\Gamma_{ijkl}^{++} - \Gamma_{ijkl}^{++}\frac{f_i^{\mathrm{eq}}(f_i^{\mathrm{eq}}+1)}{f_j^{\mathrm{eq}}(f_j^{\mathrm{eq}}+1)} - \Gamma_{ijkl}^{++}\frac{f_i^{\mathrm{eq}}(f_i^{\mathrm{eq}}+1)}{f_k^{\mathrm{eq}}(f_k^{\mathrm{eq}}+1)} + \Gamma_{ijkl}^{++}\frac{f_i^{\mathrm{eq}}(f_i^{\mathrm{eq}}+1)}{f_l^{\mathrm{eq}}(f_l^{\mathrm{eq}}+1)}\right] + \frac{1}{2}\left[-\Gamma_{ijkl}^{+-} - \Gamma_{ijkl}^{+-}\frac{f_i^{\mathrm{eq}}(f_i^{\mathrm{eq}}+1)}{f_j^{\mathrm{eq}}(f_j^{\mathrm{eq}}+1)} + \Gamma_{ijkl}^{+-}\frac{f_i^{\mathrm{eq}}(f_i^{\mathrm{eq}}+1)}{f_k^{\mathrm{eq}}(f_k^{\mathrm{eq}}+1)} + \Gamma_{ijkl}^{+-}\frac{f_i^{\mathrm{eq}}(f_i^{\mathrm{eq}}+1)}{f_l^{\mathrm{eq}}(f_l^{\mathrm{eq}}+1)}\right] + \frac{1}{6}\left[-\Gamma_{ijkl}^{--} + \Gamma_{ijkl}^{--}\frac{f_i^{\mathrm{eq}}(f_i^{\mathrm{eq}}+1)}{f_j^{\mathrm{eq}}(f_j^{\mathrm{eq}}+1)} + \Gamma_{ijkl}^{--}\frac{f_i^{\mathrm{eq}}(f_i^{\mathrm{eq}}+1)}{f_k^{\mathrm{eq}}(f_k^{\mathrm{eq}}+1)} + \Gamma_{ijkl}^{--}\frac{f_i^{\mathrm{eq}}(f_i^{\mathrm{eq}}+1)}{f_l^{\mathrm{eq}}(f_l^{\mathrm{eq}}+1)}\right]\right\}. \tag{S3}$$

for four-phonon scattering. The energy and momentum conservations of the scattering matrix are enforced by a Lagrange multiplier optimization scheme [9] to eliminate numerical errors that originate from calculations of interatomic force constants and discretization of reciprocal space.

III. Details of the first-principles calculations

The first-principles calculations are the same as in a previous work [10] that considered monolayer graphene with naturally occurring isotope concentrations and a vacuum space of 14 Å between graphene layers. We employ VASP package [11–13] and use Perdew-Burke-Ernzerhof parameterization of the generalized gradient approximation for exchange and correlation functionals [14]. The plane wave cutoff is 600 eV. For the ground state, we construct 8 × 8 × 1 supercells and use 3 × 3 × 1 k-mesh to calculate interatomic force constants (IFCs) and consider the tenth and second nearest neighboring atoms for third-order IFCs and fourth-order IFCs, respectively. We use Temperature Dependent Effective Potentials (TDEP) to account for phonon renormalization effect with stochastic sampling of the potential surface [15]. For the 300 K case, we have employed a 10 × 10 × 1 supercell of graphene, iterated the calculations using 100 thermally perturbed snapshots and the last iteration is done using 400 snapshots to ensure convergence. Three iterations are sufficient to achieve convergence in our calculations. Anharmonic temperature-dependent IFCs have the same number of many-body interactions as the ground-state IFCs. For the 100 K case, it is relatively difficult to reach the convergence, indicated by the self-consistent loop of phonon self-energy compared to previous simulations at 300 K and above, so that we take a different approach based on a geometric series with pre-conditioned iterations [16]. The convergence at 100 K is achieved at seventh iterations with 128 configurations.

IV. Convergence of calculation results on q mesh

The 40×40×1 grid in the reciprocal space is used for all Monte Carlo calculations. We test the q mesh convergence by using the iterative solution to calculate the thermal conductivity of an isotopically pure graphene ribbon with only 3-ph scattering included at 50 K. As the iterative solution for the 3-ph only case at low temperatures is known to diverge, we add an empirical boundary scattering with a width of 10 μm. The boundary scattering rate is calculated as

$$\tau_{i,\mathrm{b}}^{-1} = \frac{2|v_{i,y}|}{W} \tag{S4}$$

where $v_{i,y}$ is the group velocity in the y direction for phonon mode i. The thermal conductivity calculated with different q meshes is shown in Fig. S1. Under the constrain of boundary scattering, the variation in thermal conductivity is below 5% when the q mesh size is larger than 35×35×1. Thus, we choose 40×40×1 q mesh for all the Monte Carlo calculations, because the additional considerations of 4-ph scattering, isotope scattering, or increased temperature are expected to speed up the convergence compared to the convergence test for the 3-ph only case here.

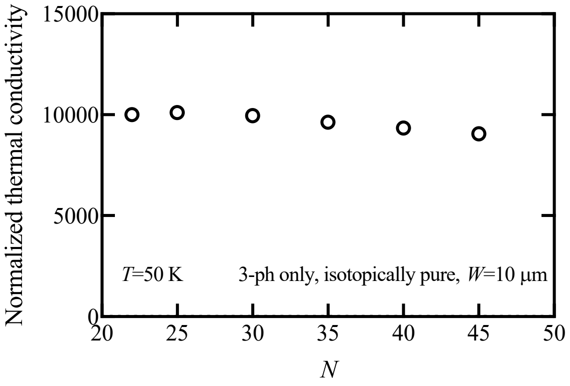

Figure S1. Calculated thermal conductivity for a 10-μm-wide, infinitely long graphene ribbon as a function of the number (N) of NxNx1 phonon wavevector (q) meshes.

IV. The effect of renormalized interatomic force constants

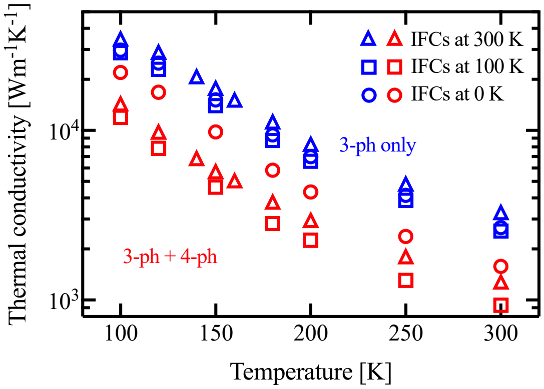

Figure S2. Monte Carlo calculations of temperature-dependent thermal conductivity for isotopically pure graphene ribbons with an infinite length and 10 μm width with IFCs renormalized at 0, 100, and 300 K.

VI. Effect of quadratic dispersion of flexural modes at small wavevector limit

According to the theoretical analysis [17], coupling of in-plane and out-of-plane atomic motions can result in linearization of the ZA modes to follow a $q^{3/2}$ instead of q^2dependence of the phonon frequency when the wavevector q is below a value q_c. The calculated q_c is about 1 nm-

^{1} at 100 K and 1.8 nm^{-1} at 300 K. In comparison, TDEP calculations of the interatomic force constants from first principles are currently limited to a supercell size of just $(10 \times 10 \times 1)$ for the graphene system due to the high computational cost. The smallest accessible wavevector with this finite simulation supercell size is 2.55 nm^{-1}, thereby excluding the long-wavelength flexural phonons that may be linearized. As a result, we do not expect that the fitted harmonic IFCs can capture the linearization of flexural phonon modes below q_c. Figure S4 shows the comparison of ZA phonon mode dispersions calculated at 0 K from DFPT and 100 and 300 K from TDEP. The x axis is along the high-symmetry path from Γ to M - for a length of $q_\mathrm{c} = 0.06q_{\Gamma\rightarrow\mathrm{M}}$. The calculated dispersions still exhibit a rather quadratic behavior for q below q_c, deviating from the predicted $q^{3/2}$ trend.

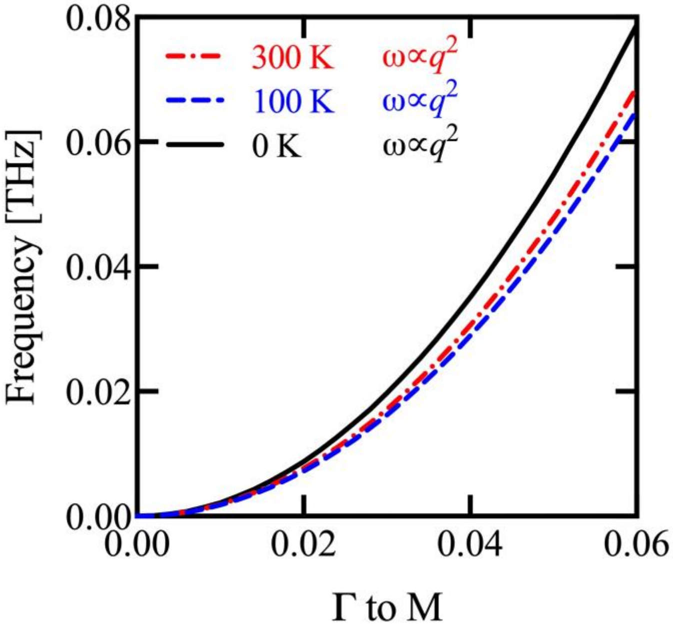

Figure S3. Comparison of phonon dispersions for flexural modes calculated at 0 K from DFPT and 100 and 300 K from TDEP.

While it remains an outstanding question whether the linearization of the long-wavelength ZA modes could increase the thermal conductivity of infinitely large suspended graphene, the contribution of these long-wavelength ZA modes is diminished by the finite characteristic size of the graphene samples considered in our study of phonon hydrodynamics. The width for the graphene ribbon reported in Fig. 2 is 10 μm, whereas the radius of the ring-shaped pump in Fig. 4 and the grating period in Fig. 5 are also 10 μm. Ballistic transport is expected in the three configurations for phonons with phonon-phonon scattering mean free paths larger than 10 μm, limiting the thermal transport contribution of these ballistic phonons. Below we provide additional calculation results to show that neglect of linearization of the flexural modes below q_{c} produces negligible effects on our calculation results for the finite-size samples.

We first calculate the ballistic thermal conductivity with an effective phonon mean free path of 10 μm for ZA phonons with a dispersion relation $\omega = aq^n$ up to q_{c}. The calculated ballistic thermal conductivity contribution at 100 K is 8.24 $\mathrm{Wm^{-1}K^{-1}}$ for a linear dispersion $(n = 1)$, 9.89 $\mathrm{Wm^{-1}K^{-1}}$ for $n = 1.5$, and 10.99 $\mathrm{Wm^{-1}K^{-1}}$ for a quadratic dispersion $(n = 2)$. Representing the upper limit of the contribution of ZA phonons with q below q_{c}, these values are expected to be larger than the error caused by an inaccurate dispersion in the calculated actual direct contribution of these long-wavelength modes. Hence, this error is negligibly small compared to our calculated thermal conductivity results in Fig. 2.

We further evaluate the effect of linearization of the long-wavelength flexural modes on the thermal conductivity contribution of other modes. Compared to a quadratic ZA dispersion, the reduced density of states of the linearized ZA modes can potentially reduce their scattering of other modes. We consider an extremely limit of the reduced density of states by completely removing flexural phonons with q below q_{c} in the calculation of the scattering rates and thermal conductivity contributions of other modes. Even at this extreme limit for infinitely large graphene, the increase in the thermal conductivity contribution calculated for other modes with a 40×40 q mesh is less than 1% when only 3-ph scattering was considered and less than 5% when both 3- and 4-ph scattering events were included. With a 10 μm boundary scattering mean free path included in the iterative solution, the change due to removing flexural phonons with q below q_{c} becomes around 1% for both 3-ph only case and 3- and 4-ph case.

These two calculation results show that neglecting the linearization of the long-wavelength ZA modes are not expected to change our conclusion on the phonon transport behaviors in these finite samples. They provide further support of our use of a 40×40 q mesh in the calculation reported in the main text. Although only the smallest q point falls below q_{c}, the numerical error is expected to be negligible because of the negligible direct and indirect contributions of these long-wavelength modes in thermal transport in the finites-size graphene samples.

VII. Heat flux profiles at 100 K

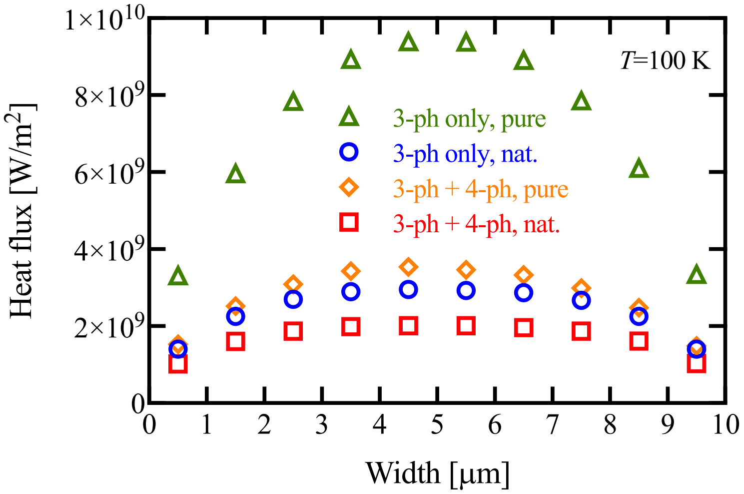

Figure S4. Heat flux profiles at 100 K for 10 μm-wide graphene ribbons under different calculation conditions.

VIII. Second sound dispersion and attenuation

The second sound dispersion and attenuation are calculated by solving the PBE with the Callaway scattering model that makes the relaxation time approximation to calculate normal and Umklapp scattering rates separately. The momentum and energy balance equations are derived from the PBE by multiplying phonon momentum and energy on both sides, respectively [18]. The balance equations are then solved with the Chapman-Enskog expansion of the distribution to first order in the Knudsen number. Assuming the displacement and temperature fields fluctuate in the form of a plane wave, the dispersion relation and attenuation of second sound are calculated [18] and shown in Fig. S5, which can be used to estimate the frequency windows and sample sizes for the second sound to be observed. For the existence of second sound, the frequency (real part of the solution) should be larger than attenuation (imaginary part of the solution) in Figs. S5(a,c). In Figs. S5(b,d), the relaxation length needs to be larger than the wavelength for the second sound to be observable in samples with a size within the gap between these two fundamental length scales.

Based on Fig. S5(a) with only 3-ph scattering at 100 K, the frequency window for second sound, which is the frequency difference between the two intercepts between the solid and dashed curves, is large, ranging over two orders of magnitude from 10 MHz to 3 GHz. The difference between the real and imaginary solutions is maximized at a frequency of approximately 0.5 GHz, which is optimal for second sound to be observed and used to choose the pulse width as the inverse of this frequency in subsequent MC simulations. Inclusion of 4-ph scattering significantly narrows the frequency window and reduces such difference, making the conditions more stringent for second sound to occur than the case with only 3-ph scattering. At 300 K, in comparison, inclusion of 4-ph scattering eliminates the window for observing second sound, which is theoretically possible over a small frequency range around 10 GHz when only 3-ph scattering is considered, as shown in Figs. S5(c,d).

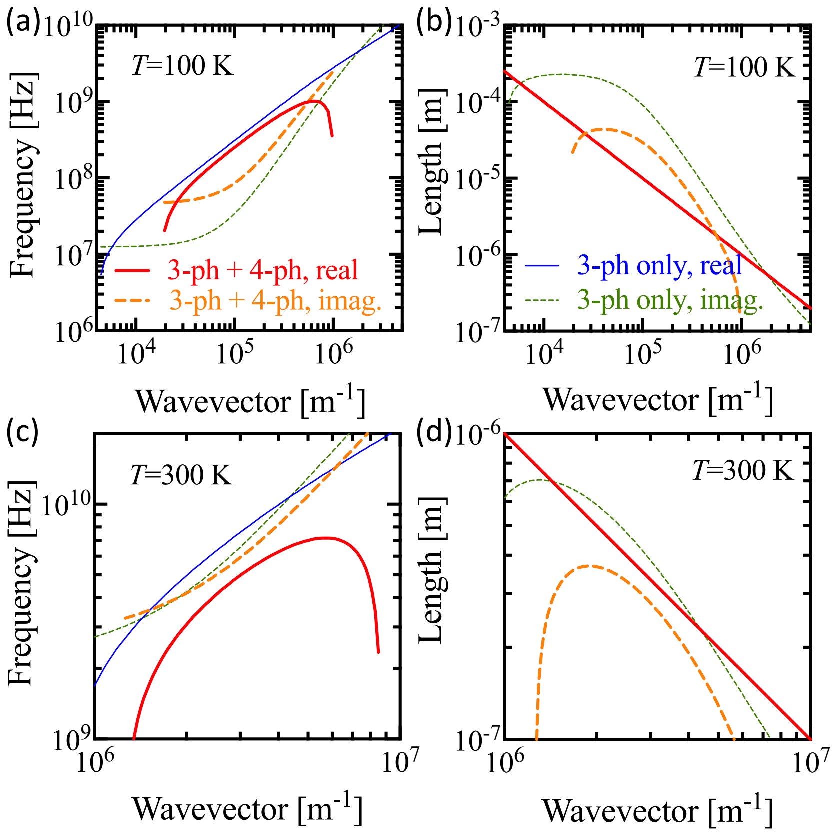

Figure S5. Second sound dispersion relation (a,c) and relaxation length (b,d) at 100 K (a,b) and 300 K (c,d). Solid curves are the real part of the solutions representing second sound dispersion in (a,c) and wavelength in (b,d). Note that the solid lines in (b,d) overlap with each other for all the four calculations specified in the legend of (a,c). Dashed curves are imaginary part of the solutions representing the attenuation in (a,c) and relaxation length in (b,d). The optimal second sound frequency is 0.5 GHz and 10 GHz at 100 K and 300 K, corresponding to optimal pause duration of 2 ns and 100 ps, respectively.

IX. Effect of the outer boundary condition

To examine the effect of the boundary condition at the two outer boundaries in the ring-shaped pump-probe thermal reflectance simulation, we have performed additional Monte Carlo simulations with a diffuse and adiabatic boundary instead of an isothermal boundary for the two outer boundaries. Figure S6 shows the comparison of the results between isothermal and adiabatic boundary conditions. We do not observe noticeable changes in the temperature peaks, the cooling effect, and oscillations between the two different boundary conditions. Only the tails of the temperature decay is extended due to the diffusely reflected phonons that add to the background diffusion signals. This result shows that the choice of isothermal boundaries has minimal effect on our results and conclusions.

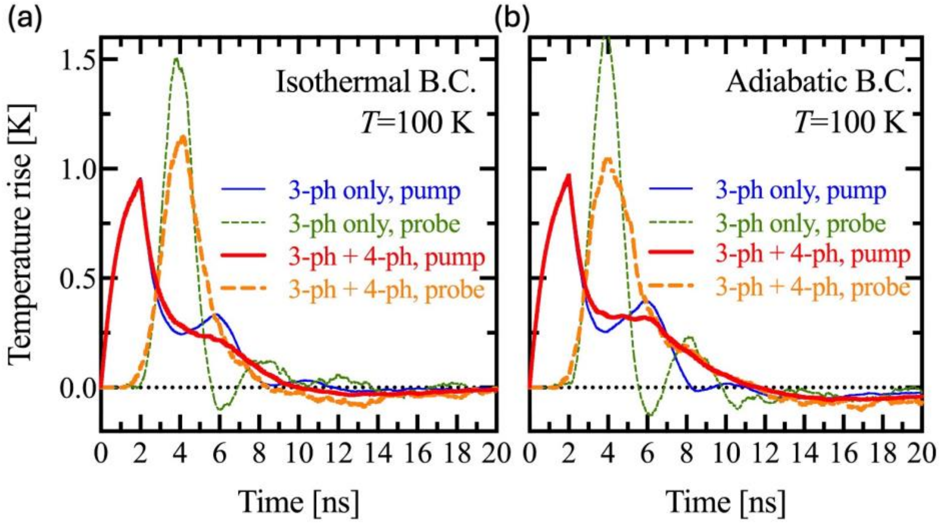

Figure S6. Transient temperature responses at the pump and probe locations at 100 K for (a) isothermal and (b) adiabatic boundary conditions.

X. Comparison with analytical solutions

To compare our simulation results with analytical solutions, we have followed a recent report [19] to use a Green's function solution to calculate the one-dimensional (1D) TTG amplitude. With a full scattering matrix and an arbitrary heat source, the Fourier transform of the temperature is given as [19]

$$\Delta\tilde{T} = \tilde{Q}\,\frac{\sum_{m,n} A^{-1}_{m,n} p_n}{i\sum_{m,n} A^{-1}_{m,n} c_n(\omega+\mathbf{q}\cdot\mathbf{v}_n)} \tag{S5}$$

where $\tilde{Q}$ is the Fourier transform of the heat source, matrix A is defined as $A_{m,n} = W_{m,n}\frac{\omega_m}{\omega_n} + i\delta_{m,n}(\omega + \mathbf{q}\cdot\mathbf{v}_n)$ where W is the scattering matrix, ω_m is the phonon frequency for mode m, ω is the temporal frequency component of the Fourier transform, $\mathbf{q}$ is the spatial wavevector from the Fourier transform, $\mathbf{v}_n$ and c_n are the phonon group velocity and heat capacity for mode n, respectively, p_n is defined as $c_n/\sum_m c_m$. Here we use m and n to represent phonon modes instead of previously used i and j, to avoid confusion with the imaginary unit i. Assuming a heating profile $Q = \bar{Q}e^{i\mathbf{q}\cdot\bar{\mathbf{r}}}\frac{sin(\omega_0 t)}{\pi t}$, we obtain the amplitude of the thermal grating as a function of time by inverse temporal Fourier transform of Eq. S5:

$$\Delta T(t) = \frac{1}{2\pi}\bar{Q}e^{i\mathbf{q}\cdot\bar{\mathbf{r}}}\int_{-\omega_0}^{\omega_0}\frac{e^{i\omega t}\sum_{m,n} A^{-1}_{m,n} p_n}{i\sum_{m,n} A^{-1}_{m,n} c_n(\omega+\mathbf{q}\cdot\mathbf{v}_n)}d\omega. \tag{S6}$$

Here, ω_0 is chosen as 2×10^9 Rad/s to obtain 2 ns as the full width of half maximum (FWHM) of the heat pulse. As ω_0 is increased further toward infinity, this expression of the heat pulse approaches the Dirac delta function. The normalized temporal TTG amplitude is then calculated as

$$\frac{\Delta T(t)}{\Delta T(t=0)} = \frac{\int_{-\omega_0}^{\omega_0}\frac{e^{i\omega t}\sum_{m,n} A^{-1}_{m,n} p_n}{i\sum_{m,n} A^{-1}_{m,n} c_n(\omega+\mathbf{q}\cdot\mathbf{v}_n)}d\omega}{\int_{-\omega_0}^{\omega_0}\frac{\sum_{m,n} A^{-1}_{m,n} p_n}{i\sum_{m,n} A^{-1}_{m,n} c_n(\omega+\mathbf{q}\cdot\mathbf{v}_n)}d\omega}. \tag{S7}$$

Figure S7(a) shows the comparison between MC simulations and analytical solution from Eq. S7 for the TTG amplitude. The two results agree well with each other regarding the frequency of the oscillation. Both methods show that 4-ph scattering reduces the damping magnitude and causes a slight delay in the oscillation. Our MC results, however, show larger magnitude in the oscillation than the analytical solution. We attribute this difference to the different pulse shape used in the MC simulation and the analytical solution. Specifically, our MC simulation considers a square pulse with a duration of 2 ns, which is more localized than the functional form used in our analytical solution to approximate the square pulse, as shown in Fig. S7(b).

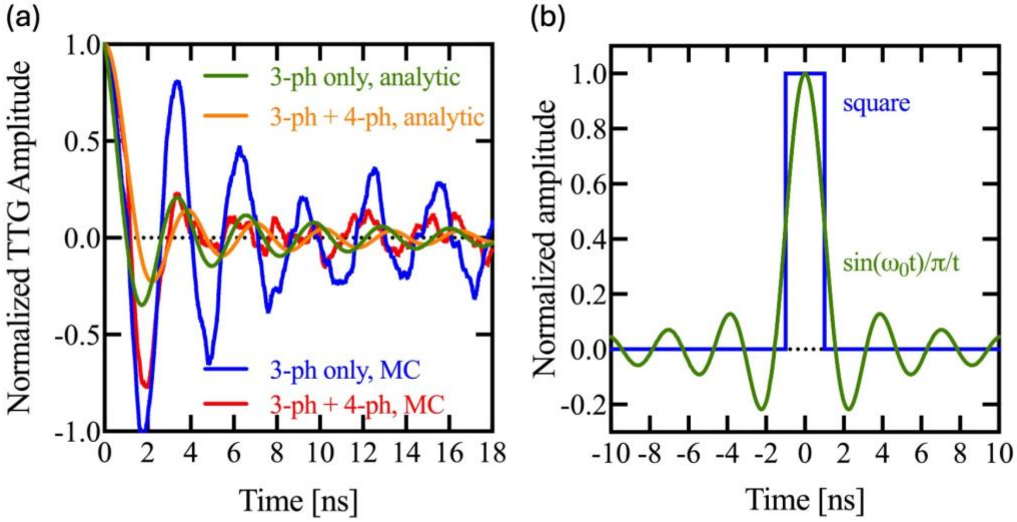

Figure S7. (a) Comparison of normalized TTG amplitude from MC simulations and analytical solutions as a function of delay time from the pulse center for 3-ph only and 3-ph + 4-ph cases. (b) Schematic plots for the square and $\sin(\omega_0 t)/(\pi t)$ pulse functions used in the MC simulation and analytical solution, respectively.

References:

[1] J.-P. M. Péraud and N. G. Hadjiconstantinou, Efficient simulation of multidimensional phonon transport using energy-based variance-reduced Monte Carlo formulations, Phys. Rev. B **84**, 205331 (2011).

[2] X. Li and S. Lee, Role of hydrodynamic viscosity on phonon transport in suspended graphene, Phys. Rev. B **97**, 094309 (2018).

[3] X. Li and S. Lee, Crossover of ballistic, hydrodynamic, and diffusive phonon transport in suspended graphene, Phys. Rev. B **99**, 085202 (2019).

[4] X. Li, H. Lee, E. Ou, S. Lee, and L. Shi, Reexamination of hydrodynamic phonon transport in thin graphite, Journal of Applied Physics **131**, 075104 (2022).

[5] J. Jeong, X. Li, S. Lee, L. Shi, and Y. Wang, Transient Hydrodynamic Lattice Cooling by Picosecond Laser Irradiation of Graphite, Phys. Rev. Lett. **127**, 085901 (2021).

[6] W. Li, J. Carrete, N. A. Katcho, and N. Mingo, ShengBTE: A solver of the Boltzmann transport equation for phonons, Computer Physics Communications **185**, 1747 (2014).

[7] Z. Han, X. Yang, W. Li, T. Feng, and X. Ruan, FourPhonon: An extension module to ShengBTE for computing four-phonon scattering rates and thermal conductivity, Computer Physics Communications **270**, 108179 (2022).

[8] C. D. Landon, A Deviational Monte Carlo Formulation of Ab Initio Phonon Transport and Its Application to the Study of Kinetic Effects in Graphene Ribbons, Massachusetts Institute of Technology, 2014.

[9] C. D. Landon and N. G. Hadjiconstantinou, Deviational simulation of phonon transport in graphene ribbons with *ab initio* scattering, Journal of Applied Physics **116**, 163502 (2014).

[10] Z. Han and X. Ruan, Thermal conductivity of monolayer graphene: Convergent and lower than diamond, Phys. Rev. B **108**, L121412 (2023).

[11] G. Kresse and J. Furthmüller, Efficiency of ab-initio total energy calculations for metals and semiconductors using a plane-wave basis set, Computational Materials Science **6**, 15 (1996).

[12] G. Kresse and J. Furthmüller, Efficient iterative schemes for *ab initio* total-energy calculations using a plane-wave basis set, Phys. Rev. B **54**, 11169 (1996).

[13] G. Kresse and D. Joubert, From ultrasoft pseudopotentials to the projector augmented-wave method, Phys. Rev. B **59**, 1758 (1999).

[14] J. P. Perdew, K. Burke, and M. Ernzerhof, Generalized Gradient Approximation Made Simple, Phys. Rev. Lett. **77**, 3865 (1996).

[15] O. Hellman, P. Steneteg, I. A. Abrikosov, and S. I. Simak, Temperature dependent effective potential method for accurate free energy calculations of solids, Phys. Rev. B **87**, 104111 (2013).

[16] N. Benshalom, G. Reuveni, R. Korobko, O. Yaffe, and O. Hellman, Dielectric response of rock-salt crystals at finite temperatures from first principles, Phys. Rev. Materials **6**, 033607 (2022).

[17] E. Mariani and F. Von Oppen, Flexural Phonons in Free-Standing Graphene, Phys. Rev. Lett. **100**, 076801 (2008).

[18] S. Lee and L. Lindsay, Hydrodynamic phonon drift and second sound in a (20,20) single-wall carbon nanotube, Phys. Rev. B **95**, 184304 (2017).

[19] V. Chiloyan, S. Huberman, Z. Ding, J. Mendoza, A. A. Maznev, K. A. Nelson, and G. Chen, Green's functions of the Boltzmann transport equation with the full scattering matrix for phonon nanoscale transport beyond the relaxation-time approximation, Phys. Rev. B **104**, 245424 (2021).